Official Journal of CIOMP
elight.springeropen.com

RESEARCH ARTICLE

Open Access

Vectorial adaptive optics

Chao He[1*†], Jacopo Antonello[1*†] and Martin J. Booth[1*]

Abstract

Adaptive optics normally concerns the feedback correction of phase aberrations. Such correction has been of benefit in various optical systems, with applications ranging in scale from astronomical telescopes to super-resolution microscopes. Here we extend this powerful tool into the vectorial domain, encompassing higher-dimensional feedback correction of both polarisation and phase. This technique is termed vectorial adaptive optics (V-AO). We show that V-AO can be implemented using sensor feedback, indirectly using sensorless AO, or in hybrid form combining aspects of both. We validate improvements in both vector field state and the focal quality of an optical system, through correction for commonplace vectorial aberration sources, ranging from objective lenses to biological samples. This technique pushes the boundaries of traditional scalar beam shaping by providing feedback control of extra vectorial degrees of freedom. This paves the way for next generation AO functionality by manipulating the complex vectorial field.

1 Introduction

Phase aberrations affect the performance of many optical systems. Adaptive optics (AO) is widely used to perform feedback correction of these aberrations in a range of applications, from the inter-galactic scale of astronomical telescopes [1] to the molecular level in super-resolution microscopy [2, 3]. However, in many systems, polarisation aberrations play an even more crucial role. These aberrations lead to polarisation errors and extra (dynamic and geometric) phase distortion (see Additional file 1: Note S1) that can be introduced, for example, when focusing through stressed optical elements, due to Fresnel's effects or induced via polarising effects in materials or biological tissues [4–7]. These effects directly alter the state of polarisation (SOP) of the light field and the focal quality, hence affecting vectorial information analysis and degrading the system resolution in ways that compound the effects of phase aberrations. Considered jointly as "vectorial aberrations" (see Fig. 1a), these polarisation and phase errors limit the performance of many vector sensitive or high-resolution optical systems.

Incorrect vector states in the illumination or detection beams are greatly detrimental for polarisation sensitive microscopes, including Stokes/Mueller confocal microscopes [7], second/third harmonic generation microscopes [8] and super-resolution fluorescence polarisation microscopy [9]. Such effects are vital, for example, to provide correct vectorial information in label-free cancer detection using Stokes/Mueller microscopy. Incorrect polarisation states also disrupt the interference at the focus, hence affecting imaging resolution. This is particularly important in sensitive super-resolution methods, for example, in the creation of the zero intensity centre of the ring-shaped STED microscopy or MINFLUX beams [10–12]; in the interference light fields of the SIM or 4Pi microscopes [13, 14]; and can also affect performance of other common microscopes [15]. Such effects would be exacerbated in deep sample imaging where there are compounded polarisation and phase errors.

As these vectorial aberrations vary with the imaging scenario, field positions, and specimen type, adaptive

†Chao He and Jacopo Antonello have contributed equally to this work.

*Correspondence:
Chao He
chao.he@eng.ox.ac.uk
Jacopo Antonello
jacopo.antonello@eng.ox.ac.uk
Martin J. Booth
martin.booth@eng.ox.ac.uk
[1] Department of Engineering Science, University of Oxford, Parks Road, Oxford OX1 3PJ, United Kingdom

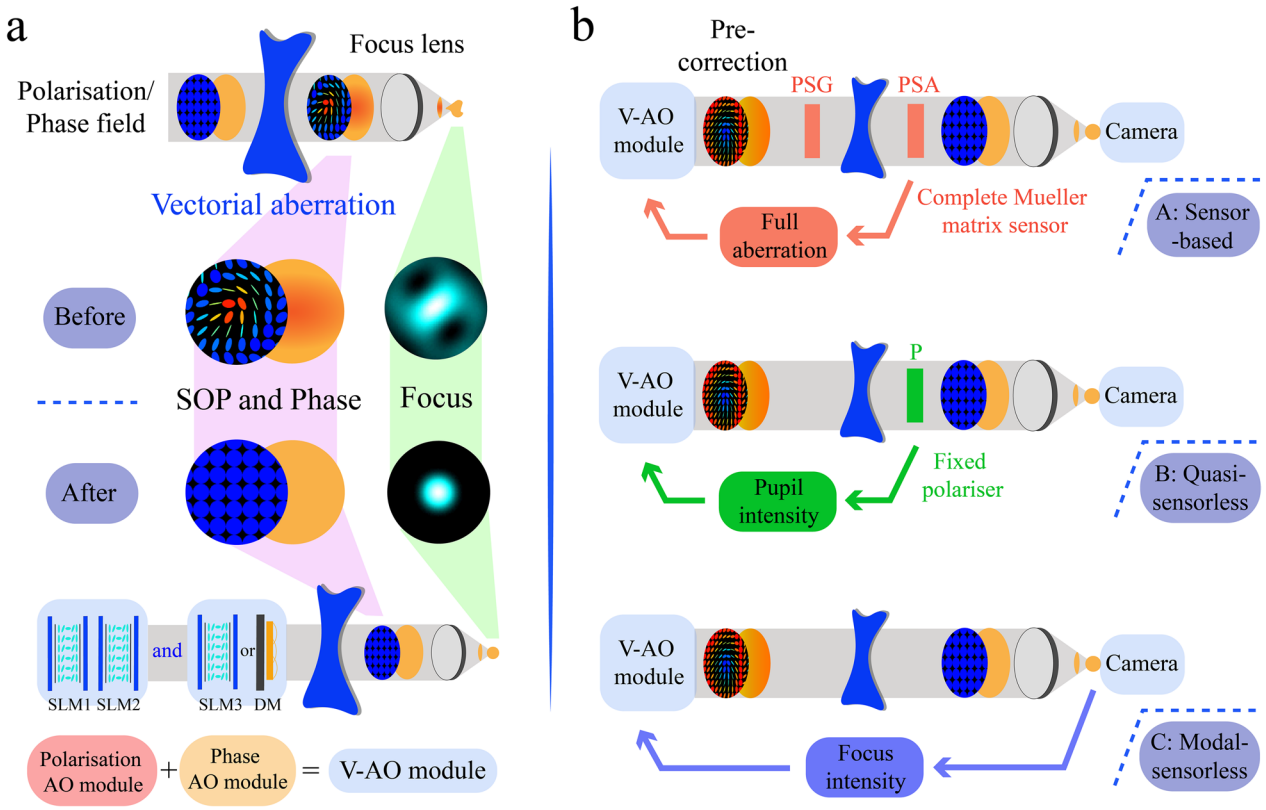

Fig. 1 Vectorial aberrations, vectorial adaptive optics (V-AO), and correction methods ranging from sensor-based to sensorless. **a** Schematic of a system affected by vectorial aberration and a V-AO compensated system. The V-AO module encompasses a polarisation module and a phase module. Here the V-AO module pre-corrects the vectorial aberration. The state of polarisation (SOP) and phase profiles, as well as focus profile are given as sketches illustrating states 'before' and 'after' V-AO correction. **b** Sketches of three different V-AO correction methods. Method A (sensor-based V-AO): A MM sensor is used to measure the aberration then give feedback to V-AO module for pre-correction, hence leading to the desired light field output. *PSG* polarisation state generator, *PSA* polarisation state analyser. Method B (quasi-sensorless V-AO): A polariser filters the intensity before the pupil, and the pupil intensity profile detected on a camera after the polariser serves as feedback for V-AO module to correct the aberration (the full setup is detailed in Additional file 1: Note S1). P: Polariser. Method C (modal-sensorless V-AO): Focal intensity is used as proxy for optimising the output phase and SOPs of the beam hence completing the V-AO loop

feedback correction is essential to obtain optimal system performance. We therefore need to extend the concepts of conventional AO to the joint compensation of polarisation and phase aberrations through introduction of the concept of vectorial adaptive optics (V-AO). Conventional phase AO requires a method of phase measurement—either through a wavefront sensor or indirect optimisation methods ("sensorless AO" for short) [2, 3]—to determine the input aberration and a method of phase compensation; whereas V-AO requires the sensing and correction of the vectorial aberration. There are significant challenges in extending existing AO methods to this higher-dimensional analogue to conventional phase correction.

In order to meet these challenges, we have implemented and validated V-AO correction through three methods: (A) sensor-based, (B) quasi-sensorless, (C) modal-sensorless; conceptual sketches of the feedback process are shown in Fig. 1b. We describe in detail the three methods and their properties, with demonstrations of the improvement of both vector field and focus after correction of commonplace vectorial aberrations. Our results indicate that V-AO can suppress vectorial aberrations, thus enhancing the toolbox for applications beyond those of traditional AO.

2 Results

In contrast to conventional AO, V-AO requires a method to determine the full vectorial properties, encompassing polarisation and phase, and a mechanism for its control. Conventional Mueller matrix (MM) polarimetry plays a role here, as the "sensor" for determination of the MM (which is equivalent to the polarisation aberration) as well as the output state of polarisation (SOP). Sensorless

V-AO methods can also be employed, allowing for example model-based optimisation of focal quality through adjustment of polarisation and phase states. Based on these principles, we introduce a suite of V-AO techniques that can be applied in different situations. Central to this is a versatile vectorial field compensation system consisting of two liquid crystal spatial light modulators (SLMs) to fully control the output SOP [16, 17] and a deformable mirror (DM) to compensate for phase (Fig. 1a) [2, 3]. Similar multi adaptive element systems have been used for the purpose of complex beam generation [18–20], whereas here we emphasise the use of such manipulators as the aberration corrector in a feedback AO system.

2.1 Sensor-based vectorial adaptive optics (Method A)

At the heart of the sensor-based V-AO implementation is an imaging MM polarimeter, which is able to extract the full polarisation properties across the profile of a beam or an object [7] (Fig. 1b). A complete MM polarimeter consists of a polarisation state generator (PSG) and a polarisation state analyser (PSA) [7]. Following the MM measurement of the object using the PSG and PSA, the SLMs are set such that the output SOP after propagation through the object is spatially uniform. This is achieved by setting the patterns displayed by precisely calibrated SLMs (see Additional file 1: Note S2), so that the SLMs introduce a pre-compensation aberration, leading to uniform output SOP. Phase aberration can also be introduced by the object, while additionally further phase variations are introduced by the SLMs themselves [21] (see Additional file 1: Note S1). Full correction is achieved by first correcting the SOP aberration using the SLMs and then applying phase only correction via conventional sensorless AO.

To illustrate some peculiarities of full vectorial aberrations (comprising both SOP and phase) we first introduce a vectorial aberration using the V-AO module. Three notable cases are depicted in Fig. 2a: (1) a beam with a uniform SOP was perturbed by such an aberration (V-AO off), resulting in both a disordered SOP in the pupil as well as a distorted focus. (2) (Phase AO on) we applied phase-only sensorless AO with the DM which results again in an aberrated focus. This verifies that traditional phase-only AO cannot fully compensate a full vectorial aberration, because a disordered polarisation state affects the constructive interference required for perfect focussing [22]. (3) Finally, the initial vectorial aberration introduced by the V-AO module is removed as following the correction procedure, resulting in a spatially near-uniform SOP in the pupil and a diffraction limited focus (V-AO on). We illustrate in Fig. 2b on the Poincaré sphere the distribution of the SOP in along a line in the cross-section of the pupil as well as cross-sections of the foci in Fig. 2a. Corresponding theoretical validation and simulations can be found in Additional file 1: Note S1. The well-matched results (for simulation and experiments) also validated the capabilities of V-AO approach.

We then chose a graded index (GRIN) lens for demonstration of a real vectorial aberration. GRIN lenses are widely used for compact imaging systems and microscopy; applications span across connectors for quantum chips to biopsy probes for clinical diagnosis. By nature of their manufacture, GRIN lenses suffer from a rotationally symmetric birefringence variation that is concomitant with their symmetrical graded index profile [4]. This property is considered as a nuisance as it introduces a vectorial perturbation that disrupts GRIN lens based imaging systems [4]; these perturbations cannot be compensated via traditional phase AO. Therefore, widespread adoption of GRIN optics is hindered in sensitive systems, such as for compact super-resolution or polarisation contrast imaging systems [4]. Similar experiments are conducted following the same process in Fig. 2a. Figure 2c shows results comparing before (V-AO off) and after correction (V-AO on). The vector fields, the correction patterns on the DM, as well as focal spot comparisons are given. More detailed analysis and quantitative data with comparisons can be found in Additional file 1: Notes S1 and S3.

These demonstrations show that the feedback sensor-based V-AO method (method A) can improve the performance of an optical system both in terms of uniformity of the SOP in the pupil and distortions at the focus.

The MM polarimeter provided complete information about the spatially variant polarising properties of the aberrating object and this information was used to apply the SOP correction in method A. However, it is also possible—and indeed sometimes more practical for various applications [2, 3]—to infer the necessary vectorial correction using less direct methods that do not require full knowledge of the polarisation aberration. We investigate here these polarimeter-free methods through the concept of "sensorless V-AO", which is named in analogy to wavefront-sensorless AO, which performs phase correction without the use of a wavefront sensor [2, 3]. In one case, a sequence of intensity measurements is taken in a conjugated pupil plane using a simple system consisting of polariser and a camera ("quasi-sensorless V-AO"; Method B); in the other case, a sequence of intensity measurements is taken at the focal plane instead of the pupil ("modal-sensorless V-AO"; Method C); see Additional file 1: Note S4. In both cases, a process is employed in order to optimize the intensity as a proxy for the uniformity of the polarisation state.

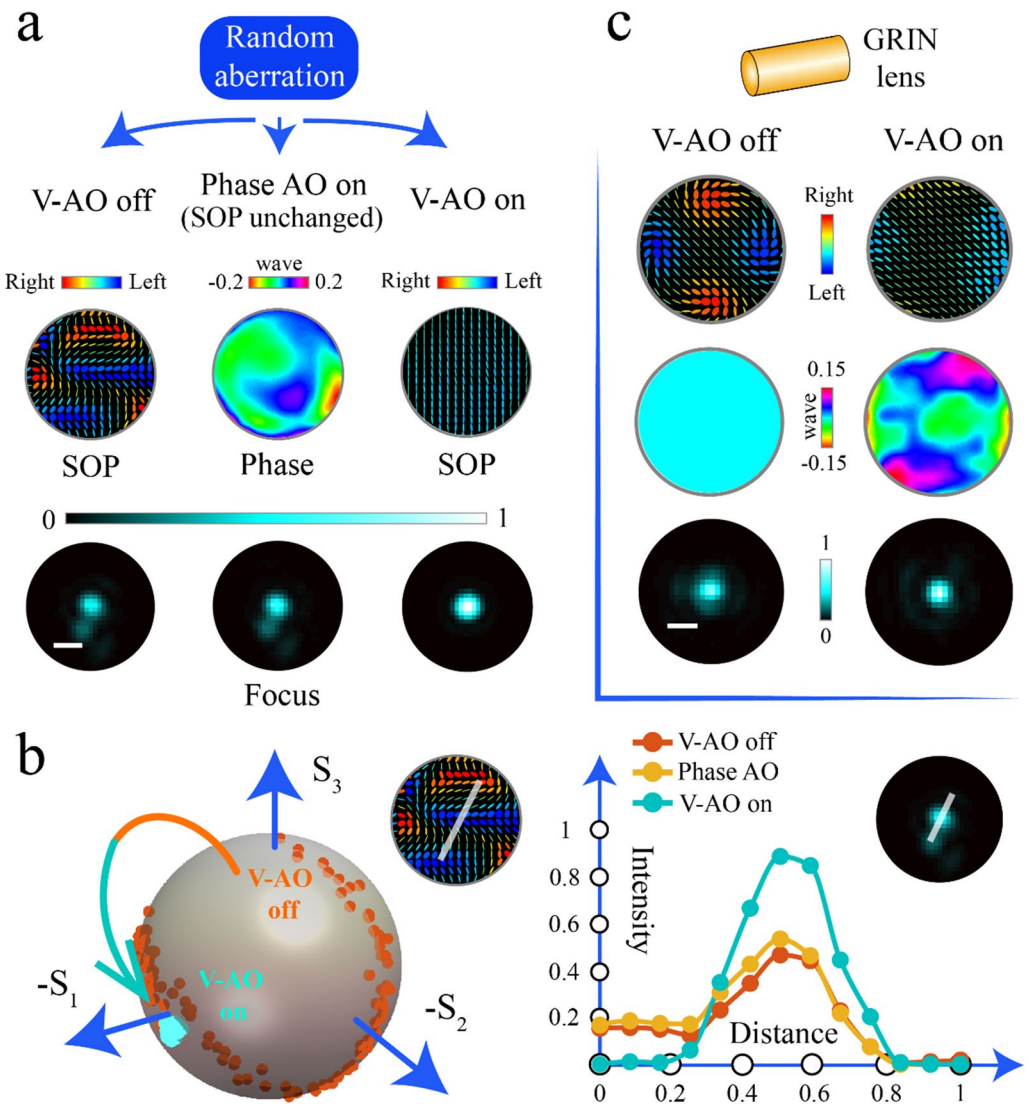

Fig. 2 Method A—sensor-based vectorial adaptive optics. **a** Random aberration case, showing V-AO off, phase AO only, and V-AO on. The vector field SOP profile, phase on the DM, profile of the foci are given. **b** SOP comparison on the Poincaré sphere of a sampled line of the vector fields of V-AO on and off status. Intensity comparison of a sampled line of different focus is presented as well. **c** V-AO off vs. V-AO on status of aberration correction for the GRIN objective lens. SOP distributions, DM phase patterns, and focus spot profiles are given. The red side of the colormap used for the SOP illustration represents right handedness while blue side is left handed. The ellipticity is illustrated via the shape of the ellipse. Pure linear SOP is shown as a green line with appropriate orientation

2.2 Quasi-sensorless vectorial adaptive optics (Method B)

Figure 3a gives a schematic of method B. At the heart of this method is the maximisation of intensity measured after a polariser across every point in the beam profile (highest intensity (HI); Fig. 3a). The camera is located at the pupil plane and measures the intensity of the output field after projection through a polariser, which was chosen to have the same principal polarisation eigenvector as the desired state (in principle, this could be spatially variant, but here linear polarisation is chosen for simplicity). When the output SOP is parallel to the eigenvector of the polariser, the intensity is maximum. One can thus correct the SOP aberration by maximizing the intensity at each point in the pupil.

For each point in the pupil, there is hence an input Stokes vector SV' that maximises the detected intensity and any other state will result in a reduced intensity. This intensity can be mapped onto the surface of the Poincaré sphere (see Fig. 3a). The point with maximum intensity corresponds to the eigenvector of the analyser and hence indicates the optimal SV' pre-correction that must be applied with the V-AO module.

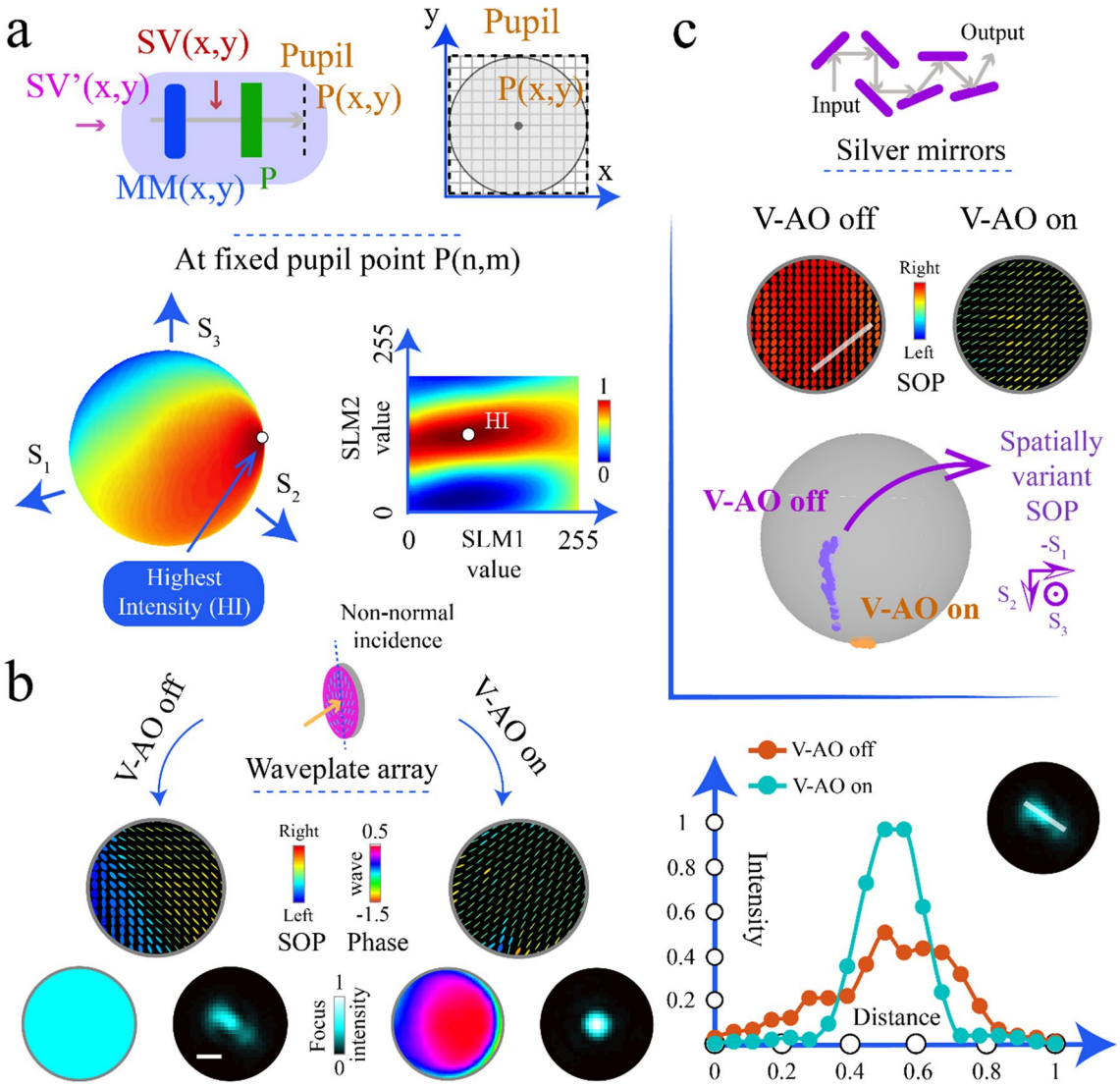

Fig. 3 Method B—quasi-sensorless vectorial adaptive optics. **a** Optimisation of SV'(x,y), which represents a Stokes vector that varies across the pupil, which is located before the aberration described by the Mueller matrix MM(x, y) and is thus related to the transformed Stokes vector SV(x, y). For a fixed point in the pupil P(n, m), the intensity is mapped onto the Poincaré sphere as function of SV'(n, m). The intensity at the same point is equivalently mapped onto a graph of the SLM pixel values. The correction mechanism involves interpolation to the maximum intensity point through a sequence of measurements using different SV'(m,n). The detailed mechanism is elaborated in Additional file 1: Note S5. **b** V-AO off vs. V-AO on status with a tilted waveplate array. SOP distributions, DM phase patterns, foci profiles, and an exemplar for comparison are given. **c** Comparison of V-AO off and V-AO on status for an assembly of protected silver mirrors. SOP distributions and Poincaré sphere comparisons are given, showing compensation of the significant errors introduced by the mirrors

In practice, this optimal correction can be obtained by sampling a number of trial configurations of the retardance settings of the two SLMs and by interpolating between these measurements to reach the maximum intensity (see exemplar in Fig. 3a). This process can also be carried out in parallel for each single point in the pupil. Detailed algorithms are elaborated in Additional file 1: Note S5. This procedure to optimise the final SV correction introduces additional phase errors due to the SLMs. This necessitates the second correction step consisting of a conventional phase sensorless AO procedure.

We validated the experimental feasibility of method B using a titled waveplate array as the aberrating object. Such a waveplate array is widely used to generate vector vortex beams, such as for the depletion focus in a STED microscope [23]. We show the state before (V-AO off) and after correction (V-AO on) including the SOP fields, the phase on the DM, the focal spots (Fig. 3b). The improvement in performance is also exemplified through comparison of focal spot intensity profiles. A further demonstration showed compensation of the deleterious vectorial effects of a series of protected silver mirrors. These standard components of various modern optical systems show problematic vectorial aberrations, due to off-axis reflections, Fresnel's effects, and coating properties [6]. We applied V-AO correction through method B, providing the results of Fig. 3c. More detailed analysis of these and other vectorial aberrations due to other optical components, such as beam splitters, wavelength filters, etc., are given in Additional file 1: Note S6. We emphasise that the aberrations corrected here are spatially variant and thus require the complex correction provided by V-AO.

2.3 Modal-sensorless vectorial adaptive optics (Method C)

Method B was able to correct vectorial aberrations after a short sequence of measurements at the conjugated pupil (correction of SOP) and focus (correction of phase). In this section, we demonstrate fully "sensorless" V-AO through method C. This method achieves V-AO correction with no additional hardware through focal plane measurement alone, taking advantage of prior knowledge of the nature of the vectorial aberration. There are various scenarios where assumptions can reasonably be made about the eigenmode axes of a polarising object, For example, this may occur in stressed optics, such as an endoscopic lens, which exhibits azimuthally or radially distributed birefringence axes, as determined by the intrinsic stress direction [4]; alternatively, in biological samples such as muscle tissue, where the axes follows the stress direction or the alignment direction of the intrinsic fibres [24]. While such prior knowledge about symmetry is useful, the value of retardance is often still unknown, such as due to variation from different manufacturing processes for the lens, or the state of the biological tissue [4, 7, 24], so adaptive vectorial correction is needed. Method C operates in analogy to conventional, phase-only sensorless methods, whereby different trial aberration corrections are applied in sequence and the optimal value of the correction is deduced by assessing the image quality using an optimisation metric [2, 3]. The salient difference for method C is that polarisation and phase aberration compensation are simultaneously performed with both SLMs and DM operating in concert at each step. This is a vectorial extension of phase correction through sensorless adaptive optics.

Sensorless feedback correction of both polarisation and phase is a challenging task, because of the complex interplay between them [6] when compensation is implemented using a combination of SLMs (see Additional file 1: Note S1). Furthermore, as feedback was provided solely through intensity measurements, a sequence of measurements was required to infer the necessary information for correction. We hence considered two different scenarios for method C. In scenario 1, we dealt only with an unknown polarisation aberration, assuming that the traditional phase aberration was negligible (Fig. 4a and b). At each point of the pupil, we had prior knowledge of the polarisation eigenmode axis, which we denoted by the line Q/-Q through the Poincaré sphere. The input SV (and equivalently the correction targeted SOP) was represented by point A. As the retardance value was unknown, the corrected SV T, which should be generated via the V-AO module, must lie on the circle K, which passed through A and was centred on Q/-Q.

In practice, this sensorless optimisation was implemented using vectorial modes defined over the whole pupil, which were based upon Zernike polynomials [2, 3]. The correction mechanism relied upon maximisation of the focal intensity (the process is elaborated in Additional file 1: Note S7), in a process that was a higher-dimensional analogue to sensorless phase AO. Optimising the intensity through adjustment of the modes on the SLMs provided an indirect route to optimisation of the SOP. In scenario 2 (Fig. 4c), we considered the combination of unknown polarisation and phase aberrations. Here, we first executed a phase-only sensorless correction routine to remove most of the phase aberration due to optical path differences on propagation through the aberrating sample. Then we applied a polarisation-only aberration correction, following the procedure used in scenario 1. Finally, we applied a further round of phase-only aberration correction to remove any residual phase bias. In effect, through maximisation of focal intensity, this V-AO procedure seeks uniformity of the SOP, rather than a specific SOP (see details in Additional file 1: Note S7).

Experimentally, we validated the feasibility of our method C (sensorless scenario 1) via a calibration target consisting of a region of birefringent material made from a piece of thin film waveplate). This creates a pure polarisation aberration with negligible phase offset (Fig. 4b). Specifically, we present the final overall system axis orientation from the combined effect of the V-AO module and the object. This in effect determines the overall system performance, as an alternative evaluation of our V-AO performance. It can be seen that the effective fast/slow axis distribution show significantly improved

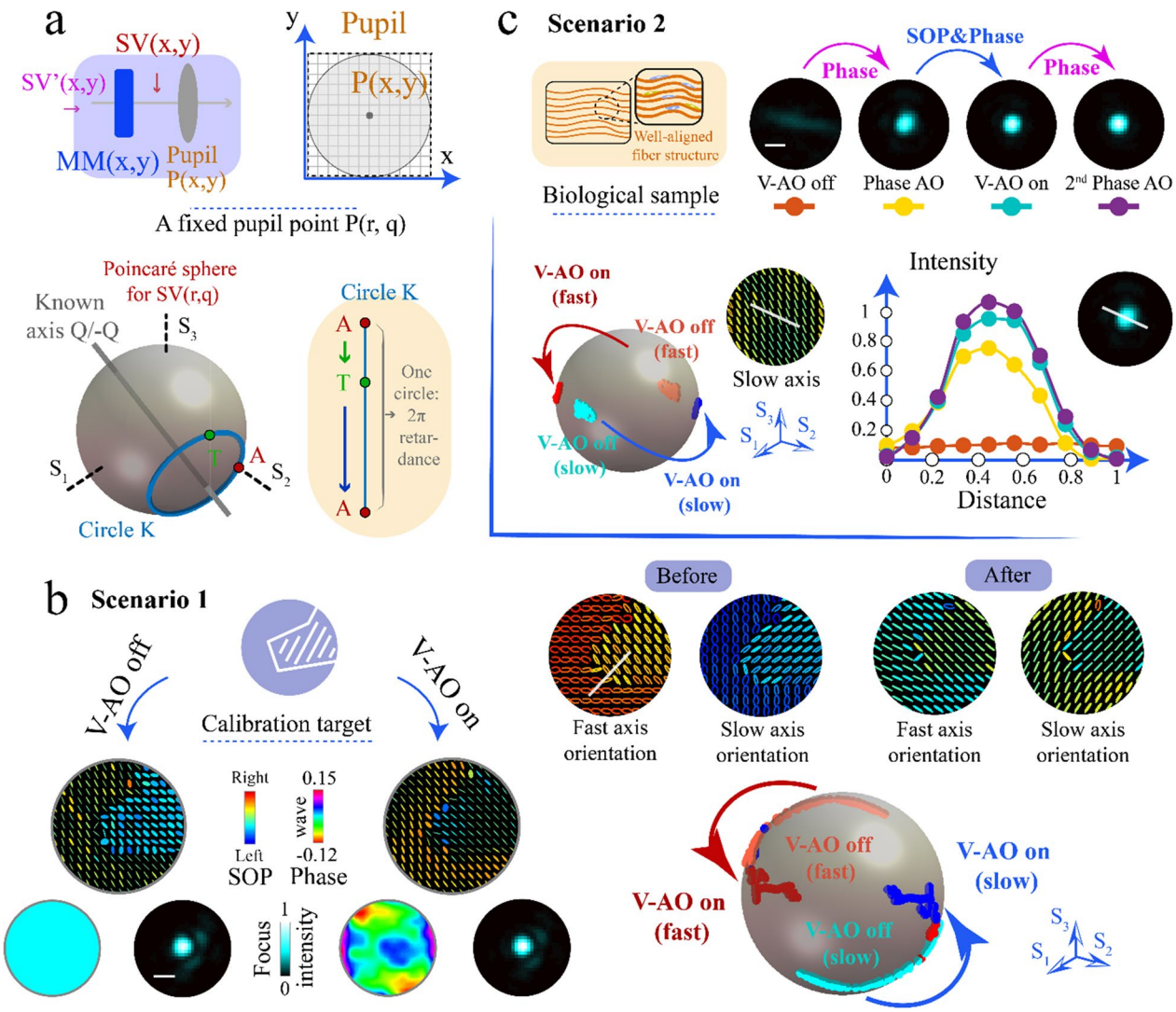

Fig. 4 Method C—sensorless vectorial adaptive optics. **a** Simplified schematic of the sensorless V-AO mechanism. Taking a fixed point P(r,q) on the pupil as example, when the axis of the aberration corresponding to this point is known, the circle K is determined. Hence, the vectorial correction must be found to set the input SV'(r,q), corresponding to point T, back to the desired SV(r,q) at point A. In practice, aberration modes are applied that change all of the points on the pupil P(x,y) simultaneously to optimise the focal intensity. Details are elaborated in Additional file 1: Note S7. **b** V-AO off vs. V-AO on status for a calibration target consisting of piece of thin film waveplate. SOP distributions, patterns on DM, focus profiles, overall slow/fast axis performances (before and after the correction), as well as the axis distributions and their comparison on Poincaré sphere are given. The corrected SOP is more uniform, and the focal spot is sharper. It can be also observed that both corrected axes are more uniform. The complex phase pattern here reveals the extra phase errors that introduced via AO correctors, which are a consequence of the complex interplay between phase and polarisation, and includes dynamic and geometric phases. **c** Comparison of V-AO off and V-AO on status of a biological sample. Focal spots distributions at three steps, axis orientation corrections, are given for comparison. It can be found that the axis distribution and focal spot profiles are enhanced after the correction process

uniformity after correction. More data, analysis and discussion are provided in Additional file 1: Note S7. V-AO correction for scenario 2 was undertaken using a thin tendon tissue sample, which exhibited both polarisation and phase effects, in this case with comparatively smaller polarisation aberrations (Fig. 4c). Focal spot performance and axis corrections are provided. Detailed analysis of the performance, including in terms of the vectorial modes, is provided in Additional file 1: Note S7. The above results validate that the sensorless V-AO method C has potential to be used in future applications that require precise vectorial control and correction of vectorial aberrations, where indirect optimisation is required, such as for beam shaping, focal control and imaging.

3 Discussion

In summary, we have extended the concepts of conventional phase-only AO into the vectorial domain by merging polarisation and phase aberration correction. V-AO can be implemented using feedback in a sensor-based approach using a polarimeter, or through two different implementations of "sensorless V-AO", which uses neither a MM polarimeter nor a wavefront sensor.

These three approaches provide a versatile toolkit for compensation of vectorial aberrations, which can be chosen to match conditions in real applications. The sensor-based method provides the most comprehensive approach compatible with full MM characterisation, should it be necessary. However, the quasi-sensorless (and modal-sensorless) method can provide the ability to perform V-AO with simpler hardware requirements compatible with more practical scenarios [2, 3]. The quasi-sensorless method features unique advantages: First, the complex hardware necessary for a full MM polarimeter measurement is replaced by a simple analyser without moving parts. Second, calculation of the MM is no longer needed, nor is its decomposition for application of the SLM settings, which avoids the complex error amplification due to the MM matrix calculation [7]. Third, detailed calibration of the SLMs is not necessary, as the optimization procedure can be expressed directly in terms of the pixel values applied to the two SLMs. The modal-sensorless approach requires no additional hardware and no extra pupil measurement, uses prior knowledge of the target, and is based purely on focal optimisation. These methods can separately assist different optical system scenarios, with intriguing directions that are largely unexplored.

Future developments can expand these methods to deal with light depolarised by the object, which can occur in scenarios such as bulk tissue monitoring or diagnosis [7]. Furthermore, with an increased number of AO devices, the V-AO format can be extended. The current system, using two SLM passes, can provide vectorial aberration compensation with pre-correction of the illumination state. For even wider reach, the system could be expanded to three SLM passes [17], thus permitting conjugation of the vectorial state, for example in the emission path of a microscope. More discussion and perspectives can be found in Additional file 1: Note S8.

Overall, we have put forward novel V-AO techniques for joint correction of polarisation and phase aberrations. With these vectorial field feedback control methods, this next-generation AO technique is expected to benefit various research areas—for example [25–31], ranging from astronomical telescopes to microscopy—with further applications spanning across galaxy detection, to laser-based and lithographic nano-fabrication, in addition to biomedical and clinical characterization.

Supplementary Information

The online version contains supplementary material available at https://doi.org/10.1186/s43593-023-00056-0.

Additional file 1: Figure S1. Simplified layout of the optical system used in the experimental validation. (a) A HeNe laser beam (Melles Griot, 05-LHP-171, 632.8 nm) is expanded and directed towards the first SLM (SLM1; Hamamatsu, X10468-01). After reflection the beam passes through a half-wave plate (HWP2; Thorlabs, WPH10M-633) and is reflected off the second SLM (SLM2; Hamamatsu, X10468-01) first, and then off a DM (Boston Micromachines Corporation, Multi-3.5). The planes conjugate to the pupil plane are denoted with ∅ (the telescopes that reimage these planes are not depicted for simplicity).Some positions in the setup are enumerated with numbers between parentheses in purple. The frame of reference at position (3) is used to indicate the orientation of HWP2. Measuring positive angles from the *x* towards the *y* axis, the slow and fast axes of HWP2 are at 22.5∘ and 112.5∘, respectively. Legend: HWP half-wave plate, M flat mirror, P polariser (Thorlabs, GL10-A), BE beam expander, BS beam splitter (Thorlabs, BS010), FBS flip-in beam splitter (Thorlabs, BS010), C camera (Thorlabs, DCC3240N), QWP quarter-wave plate (Thorlabs, WPQ10M-633); (b) Flip-in elements denoted by letters in (a); (c) Table showing in which cases the flip-in elements depicted (b) are enabled. **Figure S2.** Experimental validation of the modelling reported in Supplementary Note 1.1. A randomly chosen aberration is induced with both SLMs and no aberrating object is present at position (6) in Supplementary Fig. 1. (a) MM data computed using the modelling relating position (1) and position (6); (b) SOP predicted at position (6) using the modelling when $j\,1 = [1; -1]/\sqrt{2}$; (c) FID computed using the modelling and expected at camera C2; (d) Experimental MM data measured with MM polarimetry [12]; (e) SOP predicted at position (6) using the experimentally measured MM data; (f) FID measured with camera C2; (g) phase applied in the phase-only correction; (h) FID profiles for the VAO-off, phase-ony, and VAO-on states. Experimental diffraction-limited FID and prediction using the Airy disk formula. **Figure S3.** Generation of an arbitrary SOP at position (4) in the optical setup. The Stokes vectors *S* indicate the SOP at various positions in the setup, which are denoted by the number in the subscript. (a) The initial state $S1$ is fixed to $[0; -1; 0]$, whereas an arbitrary state $S4$ is desired; (b) Retardance θ1 is applied with the first SLM, which is modelled as a rotation by θ1 along the *H* axis. This is followed by a rotation of 180∘ modelling the reflection off the back plane of the SLM; (c) The effect of the half-wave plate is that of applying a rotation of 180∘ about the *W* axis; (d) The desired state $S4$ is reached using two rotations about the *H* axis modelling both the retardance θ2 applied with SLM2 and the reflection off the back plane. **Figure S4.** Correction of a GRIN lens SOP aberration. (a) Mueller matrix data obtained by measuring a cross-section of a GRIN lens using an external MM polarimetry setup described in [12]; (b)–(c) Distribution of the extra-ordinary axes and the retardance δ of the GRIN lens. Both parameters were extracted from the data reported in (a) using the procedure outlined in Supplementary Note 3. The parameters of the polarisation ellipses are retrieved [7] from the distribution of axis *Q* across the aperture. The ellipses are then plotted in (b) to visualise the orientation of the extra-ordinary axes. Note that the plot in (b) is different from the plots in Supplementary Fig. 2(b)–(c), where the SOP is visualized instead of the axes; (d) Mueller matrix data obtained after correction of the GRIN lens SOP aberration. This measurement is taken between position (1) and position (6) in Supplementary Fig. 1, and thus comprises both the pre-correction applied with the two SLMs and the aberration due to the GRIN lens. As can be seen by comparing with (a), element (3,3) has become approximately uniform, which validates the correction for the fixed input SOP $S1 = [0; -1; 0]$; (e)–(f) Distribution of the axes and retardance after correction of the GRIN lens SOP aberration. Both parameters were extracted from the data reported in (d) As can be seen by comparing (e) with (b), the axes have become approximately linearly polarised along −45∘, for which the fixed input Jones vector $j\,1 = [1; -1]/\sqrt{2}$ is an eigenvector. The retardance shown I (f) essentially becomes a

scalar aberration, which can be corrected with the DM. **Figure S5.** Additional data from the correction of a GRIN lens SOP aberration. (a) phase applied with the DM; (b) Stokes components obtained from the MM polarimetry data in Supplementary Fig. 4 shown before (VAO-off) and after (VAO-on) the SOP correction; (c) Profiles of the FID measured before and after correction and prediction using the Airy disk formula. **Figure S6.** Example showing the correction of the SOP on the Poincar´e sphere. (a) An object aberrating the SOP is represented by the Jones matrix SU2(Q, δ) and can be visualised as a rotation by an angle δ about the axis Q; (b) The optimal pre-correction Sc is found by starting from $S1$ and by applying the opposite rotation SU2(Q, $-\delta$); (c) Correction of the SOP. Starting from $S1$, the two SLMs and half-wave plate change the SOP into Sc. This is depicted as a set of rotations along the light blue paths. Subsequently, the aberrating object applies the rotation SU2(Q, δ) depicted as the yellow path, which restores the SOP to the initial state $S1$. **Figure S7.** Classification of the sensor-based and sensorless strategies for conventional phase-only AO and for V-AO. **Figure S8.** Layout of aMMpolarimeter. The PSG and PSA are highlighted in blue dotted boxes. P polariser; QWP rotating quarter-wave plate. **Figure S9.** Intermediate steps performed during the correction of the SOP for Method B. A coarse grid of pixel values tuples is initially created, see Eq. (30). For each tuple ($g1$, $g2$), $g1$ is applied to all pixels of SLM1, $g2$ is applied to all pixels of SLM2, and an image is recorded with camera C1, as outlined in Supplementary Note 5. For each pixel in the aperture, the intensity sampled from the recorded images and its interpolation are evaluated, see (a) and (b) respectively, and the maximum intensity is identified in (b). From the pixel values $g1$ and $g2$ corresponding to the maximum interpolated intensity, the correction patterns for SLM1 and SLM2 are computed, as shown in (c) and (d), respectively. **Figure S10.** Flow chart summarising the main steps for Method B outlined in Supplementary Note 5. The final correction of the phase using a sensorless method [19] is not depicted. **Figure S11.** Vectorial aberrations arising from common optical elements. (a) On the left, the retardance and diattenuation measured due to a silver mirror oriented at different angles of incidence β. On the right, the same measurements using one, two, and three pairs of mirrors oriented at 45∘; (b) Vectorial aberrations obtained from cube, plate, and pellicle beam splitters, and a bandpass filter (633 nm transmission). The measurements are performed in transmission and reflection denoted by T and R in the abscissa. **Figure S12.** Flow chart summarising the main steps for Method C outlined in Supplementary Note 7.1. **Figure S13.** Correction of the SOP aberration due to a target object. (a) Distribution of the axes of the target. This information is assumed known a priori in Method C. Parameter Q is extracted from MM polarimetry measurements, as outlined in Supplementary Note 3. From the relationship$Q = [\cos(2X)\cos(2\Psi); \cos(2X)\sin(2\Psi); \sin(2X)]$ the parameters of the polarisation ellipse are obtained [7], and the corresponding ellipses are plotted in the aperture disk; (b) Distribution of the axes of the combined pre-correction using the SLMs and the target aberrating object at position (6) after applying Method C, Scenario 1, see Supplementary Note 7.1. The axes are approximately homogeneously linearly polarised, aside from errors at the boundary, showing improvement with respect to (a). **Figure S14.** Example of fits performed for the sensorless algorithm described in Supplementary Note 7.1. (a) Measurements of the metric in blue and fit of the measurements in red for the first Zernike mode Z1; (b) Same as (a) for the fourthZernike mode Z4 [35]; In both (a) and (b), the abscissa denotes the amount of Zernike mode applied. The ordinate denotes the normalised value of the image quality metric [19] determined measuring the corresponding FID. The vertical dashed line denotes the optimal amount of mode determined after the fit. The value of $\hat{\delta}$, $\theta 1$, $\theta 2$, and ψ is annotated at some states with letters [A]–[F], see Supplementary Fig. 15 and Supplementary Fig. 16. The correction is applied incrementally, so that in (b) the correction for modes 1, 2, and 3 is already applied. **Figure S15.** State of $\hat{\delta}$, $\theta 1$, $\theta 2$, and ψ at different steps annotated by letters [A], [B], and [C] during the correction of mode 1 in Supplementary Fig. 14(a). **Figure S16.** State of $\hat{\delta}$, $\theta 1$, $\theta 2$, and ψ at different steps annotated by letters [D], [E], and [F] during the correction of mode 4 in Supplementary Fig. 14(b). **Figure S17.** Vectorial aberrations in a multi-layer object. A focussing arrangement is shown on the left where two V-AO modules A and B are highlighted in blue. An inset indicating the layers of the specimen is shown on the right.

Acknowledgements
The project was supported by the European Research Council (AdOMiS, no. 695140). C.H. was supported through a Junior Research Fellowship from St John's College, University of Oxford.

Author contributions
CH, JA and MJB originated the project and conceived the V-AO approaches. CH designed and built the experimental hardware, conducted polarimetry software, prepared the samples. CH and JA planned the simulation, implementation of both the sensor and sensorless algorithm, and conducted the experiments together. JA performed simulation and algorithm, control software and data extraction methods. JA, CH and MJB analysed the data, wrote and edited the paper. CH prepared the figures and oversaw the project together with MJB.

Declarations

Competing interests
The authors declare no competing interests.

Received: 19 September 2023 Revised: 19 September 2023 Accepted: 28 September 2023
Published online: 27 November 2023

References

1. Tuan Do et al., Relativistic redshift of the star S0–2 orbiting the Galactic Center supermassive black hole. Science **36**(6454), 664–668 (2019)
2. M.J. Booth, Adaptive optical microscopy: the ongoing quest for a perfect image. Light Sci. Appl. **3**(4), e165–e165 (2014)
3. Na. Ji, Adaptive optical fluorescence microscopy. Nat. Methods **14**(4), 374–380 (2017)
4. C. He et al., Complex vectorial optics through gradient index lens cascades. Nat. Commun. **10**(1), 1–8 (2019)
5. Patrick S. Salter, Martin J. Booth, Adaptive optics in laser processing. Light Sci. Appl. **8**(1), 1–16 (2019)
6. R.A. Chipman, W.-S.T. Lam, G. Young, *Polarized light and optical systems* (CRC Press, Boca Raton, 2018)
7. C. He et al., Polarisation optics for biomedical and clinical applications: a review. Light Sci. Appl. **10**(1), 1–20 (2021)
8. J. Morizet et al., High-speed polarization-resolved third-harmonic microscopy. Optica **6**(3), 385–388 (2019)
9. L. Chen et al., Advances of super-resolution fluorescence polarization microscopy and its applications in life sciences. Comput. Struct. Biotechnol. J. **18**, 2209–2216 (2020)
10. X. Hao et al., Three-dimensional adaptive optical nanoscopy for thick specimen imaging at sub-50-nm resolution. Nat. Methods. **18**(6), 688–693 (2021)
11. X. Hao et al., Effects of polarization on the de-excitation dark focal spot in STED microscopy. J. Opt. **12**(11), 115707 (2010)
12. K.C. Gwosch et al., MINFLUX nanoscopy delivers 3D multicolor nanometer resolution in cells. Nat. Methods **17**(2), 217–224 (2020)
13. J. Wang et al., Implementation of a 4Pi-SMS super-resolution microscope. Nat. Protoc. **16**(2), 677–727 (2021)
14. M. Žurauskas et al., IsoSense: frequency enhanced sensorless adaptive optics through structured illumination. Optica **6**(3), 370–379 (2019)
15. F. Kenny et al., Complete polarization and phase control for focus-shaping in high-NA microscopy. Opt. Express **20**(13), 14015–14029 (2012)
16. Y. Dai et al., Active compensation of extrinsic polarization errors using adaptive optics. Opt. Express **27**(24), 35797–35810 (2019)
17. Q. Hu et al., Arbitrary vectorial state conversion using liquid crystal spatial light modulators. Opt. Commun. **459**, 125028 (2020)
18. C. Rosales-Guzmán, B. Ndagano, A. Forbes, A review of complex vector light fields and their applications. J. Opt. **20**(12), 123001 (2018)
19. J. Wang, F. Castellucci, S. Franke-Arnold, Vectorial light–matter interaction: exploring spatially structured complex light fields. AVS Quantum Sci. **2**(3), 031702 (2020)

20. H. Rubinsztein-Dunlop et al., Roadmap on structured light. J. Opt. **19**(1), 013001 (2016)
21. Q. Hu, C. He, M.J. Booth, Arbitrary complex retarders using a sequence of spatial light modulators as the basis for adaptive polarisation compensation. J. Opt. **23**(6), 065602 (2021)
22. M. Born, W. Emil, *Principles of optics: electromagnetic theory of propagation, interference and diffraction of light* (Elsevier, Amsterdam, 2013)
23. Z. Rong et al., Super-resolution microscopy based on fluorescence emission difference of cylindrical vector beams. Opt. Commun. **354**, 71–78 (2015)
24. H. He et al., Monitoring microstructural variations of fresh skeletal muscle tissues by Mueller matrix imaging. J. Biophotonics **10**(5), 664–673 (2017)
25. J.B. Breckinridge, W.S.T. Lam, R.A. Chipman, Polarization aberrations in astronomical telescopes: the point spread function. Publ. Astron. Soc. Pac. **127**(951), 445 (2015)
26. H.B. de Aguiar, S. Gigan, S. Brasselet, Polarization recovery through scattering media. Sci. Adv. **3**(9), e1600743 (2017)
27. T. Čižmár, K. Dholakia, Exploiting multimode waveguides for pure fibre-based imaging. Nat. Commun. **3**(1), 1–9 (2012)
28. T. Novikova et al., Special Section guest editorial: polarized light for biomedical applications. J. Biomed. Opt. **21**(7), 071001 (2016)
29. D. Sinefeld et al., Adaptive optics in multiphoton microscopy: comparison of two, three and four photon fluorescence. Opt. Express. **23**(24), 31472–31483 (2015)
30. N.A. Rubin et al., Matrix Fourier optics enables a compact full-Stokes polarization camera. Science **365**(6448), 6448 (2019)
31. X. Bai, et al., Polarization-based underwater geolocalization with deep learning. eLight **3**(1), 15 (2023)